Received: 1 June 2022 | Revised: 30 January 2023 | Accepted: 2 June 2023

DOI: 10.1111/str.12455

RESEARCH ARTICLE

strain WILEY

Application of high-performance DIC for a comprehensive evaluation of biaxial fatigue crack growth experiments

Andreas Blug[1] | **Fabian Conrad**[2] | **Alexander Bertz**[1] | **Christian Kontermann**[2] | **Daniel Carl**[1] | **Matthias Oechsner**[2]

[1]Fraunhofer Institute for Physical Measurement Techniques IPM, Freiburg, Germany

[2]Institute for Materials Technology IfW, Technical University of Darmstadt, Darmstadt, Germany

Correspondence
Andreas Blug, Fraunhofer Institute for Physical Measurement Techniques IPM, Georges-Köhler-Allee 301, 79110 Freiburg, Germany.
Email: andreas.blug@ipm.fraunhofer.de

Funding information
Federal Ministry for Economic Affairs and Climate Action (BMWK), Grant/Award Number: IGF no. 20239 N

Abstract

Precise determination of the remaining service life of technical components requires sufficient knowledge of fatigue crack growth behaviour and the growth rate of defects. Cracks in real components often experience multiaxial far field stresses due to their complex geometry and composite loadings acting on it. Digital image correlation (DIC) is well established for crack length and displacement measurements, but it usually requires sample preparation with speckle paint and interferes with mechanical extensometers. To overcome these limitations, we use a novel 2D DIC system combining a graphics processing unit (GPU) with a CoaXPress 2.0 camera, acquiring up to 3 GB/s of image data. It enables real-time evaluation of both integral strain like an extensometer and full-field DIC on images selected automatically in real-time. This combination enables the use of one single sensor for strain-controlled testing and fatigue crack growth characterisation. The full-field displacement is compared to a finite-element model (FEM) simulating the actual crack contour measured by the DIC system. The results show that high-performance DIC has the potential to simultaneously simplify crack-growth experiments and provide comprehensive fracture mechanical information.

KEYWORDS

digital image correlation, fatigue crack growth, finite-element model, strain-control, uni- and biaxial loading

1 | INTRODUCTION

Precise determination of the remaining service life of technical components requires sufficient knowledge of fatigue crack growth behaviour and the growth rate of defects. Cracks in real components often experience multiaxial far field stresses due to their complex geometrical shape and composite loadings acting on it. However, fatigue crack growth laws are derived in laboratory experiments almost exclusively using uniaxially loaded specimens. The precise influence of multiaxial far-field loadings on the fatigue crack growth behaviour is neither fully understood nor experimentally examined with a standard fatigue crack growth specimen. This paper describes a high-performance digital image correlation (DIC) system specifically designed for a planar biaxial test-rig to carry out multiaxial fatigue crack growth

experiments. The focus of the biaxial investigation is on fatigue crack growth rate, plasticity-induced crack closure and crack growth direction.

ASTM E 647 comprehensively describes the determination of fatigue crack growth rates for various uniaxial test configurations in the Paris regime.[1] Basically, these trials are equipped with sensors measuring crack length a with a precision of 0.1 mm (1 σ), a counter for cycles N and a force and displacement measurement resolving the so-called compliance, that is, the slope of the strain or displacement perpendicular to the crack driving force, with 2% of the cycle force range. This requirement is quite similar to the 1% resolution recommended by ASTM E 606 for strain-control.[2] In Paris regime, the crack growth rate da/dN is driven by the cyclic stress intensity factor ΔK which is a function of crack length a, force F and the crack geometry. Within experiments, ΔK can be controlled in different ways: force-controlled, in the simplest case or strain-controlled, in order to be closer to component-loading cases and typically available fatigue data. Instead of ΔK, the effective cyclic stress intensity factor ΔK_{eff} considering crack opening/closing can be used when plasticity-induced crack closure is prevalent. For a standard uniaxial specimen, K can be calculated using either analytical or tabular finite-element model (FEM) solutions from the literature.[1] For more complex crack growth specimens or complex-shaped components, the actual value of K has either to be calculated from time-consuming FEM simulations or measured from full-field DIC measurements.[3]

As full-field DIC measures similar strains and displacements as they are calculated by fracture mechanical FEMs, the combination of both appears ideal to gain the maximum amount of information out of fracture mechanic testing, like the remnant-lifetime assessment of materials utilised in the Paris regime.[4,5] However, these methods have certain short falls: First, neither full-field DIC nor FEM are real-time methods—so they are not useful for process control during crack growth. As a consequence, the experiment must be interrupted, leading to extraneous errors like temperature-induced relaxation effects and significantly increased time and handling effort. Second, full-field DIC and FEM require different grid geometries, leading to compromises in measurement accuracy, model complexity and application of boundary conditions. Alternatively, methods like crack opening displacement (COD) or J-integral have been developed for a direct assessment of K from full-field DIC.[6,7] However, under mixed-mode conditions, they are still under research.[8] All these methods require clear recognition of the crack tip itself. However, there is only a little literature on the automatic evaluation of crack tip position on curved paths under biaxial conditions.[9–11]

Real-time DIC data processing is challenging due to the enormous computational load of the related algorithms. Therefore, graphics processing unit (GPU)-based 2D and 3D implementations have become increasingly popular in recent years,[12] with almost all of them concentrating on full-field evaluations. Without GPU, even integral strain measurement rates correlating only two or four subsets hardly exceed 100 Hz.[13–17] In this paper, we report the expansion of an implementation originally designed as a real-time extensometer measuring integral strain for comprehensive crack growth evaluation.[13,18] According to the scheme of Thiagu, it uses in-subset parallelism for the FFT-CC algorithm on the GPU with zero-order shape functions. The latter restricts its applications to those with negligible shear deformation within the subset—like fatigue in metals, where strain is usually well below 1%. This restriction avoids iterative data processing, resulting in low latencies in the range of 2 ms.[18]

This paper emphasises the question of how GPU-based high-performance DIC computing can be used for a rather simple but comprehensive workflow for crack growth experiments. After introducing the cruciform specimen and alternating current potential drop (ACPD) as reference method for crack length measurements, the current DIC sensor with the evaluation workflow is described. Starting with Section 6, methods to determine crack paths and crack tip positions in full-field DIC are discussed, including a comparison between DIC and a standard FE model for the calculation of ΔK from the DIC crack path. Finally, Paris diagrams for a titanium alloy measured by DIC and by ACPD are compared.

As published previously, the approach in this paper is suitable for uniaxial and biaxial trials.[19] Results discussed here are an overview of different biaxial measurements from a series analysing the influence of multiaxial stresses on the fatigue crack growth rate, the plasticity-induced crack closure and the mutual influence of HCF-LCF cycle combinations. Systematic fracture mechanical evaluations for each material are discussed in separate publications.[20–22]

2 | BIAXIAL SPECIMEN AND LOADING SCENARIOS

The experimental campaign uses a cruciform specimen in combination with a planar biaxial test rig to analyse the influences of multiaxial loadings on fatigue crack growth. In contrast to uniaxially loaded standard specimen, the cruciform ones have two loading axes, A and B. The specific geometry is depicted in Figure 1. The total width is 110 mm, with a thickness of 8 mm in the clamping area. A defined multiaxial stress state is induced in the centre of the specimen

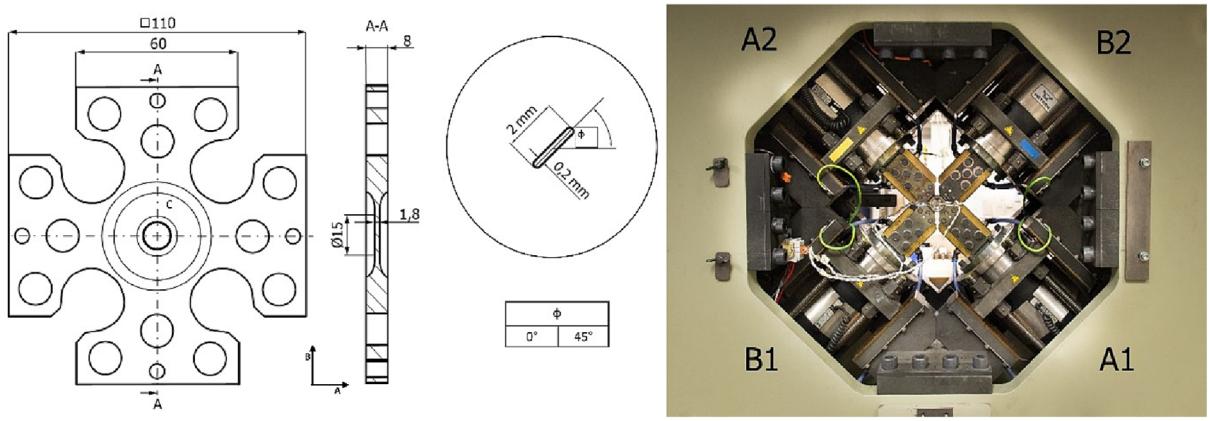

FIGURE 1 Cruciform specimen for biaxial loading (left). Detail C outlines the orientation of the crack-starter notch. Right: Biaxial testing machine. The digital image correlation (DIC) sensor head shown in Figure 2 is mounted on the back side of the frame.

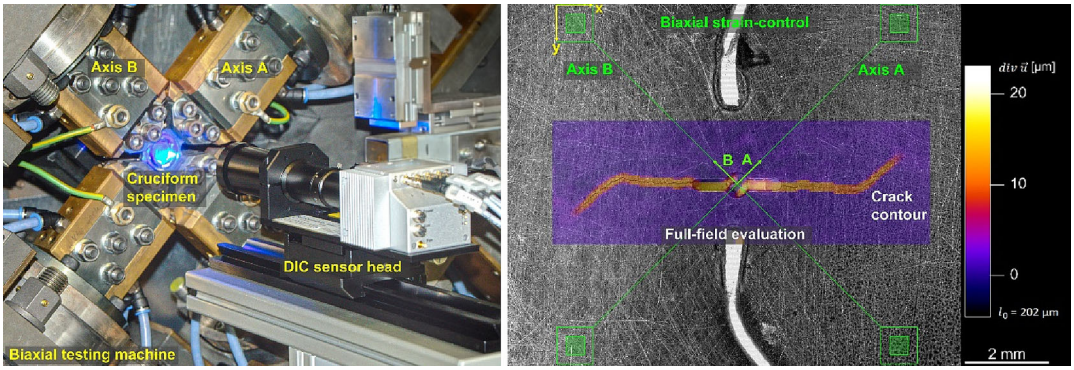

FIGURE 2 Left: digital image correlation (DIC) sensor head in front of the biaxial testing machine equipped with a cruciform specimen. Right: camera image of specimen surface superimposed by the four subsets for strain-control and by the full-field evaluation area. The (x,y) coordinates (yellow) mark the camera coordinate system, and the (A,B) coordinates correspond to the A and B axes of the biaxial testing system.

TABLE 1 Loading scenarios for force-controlled fatigue crack growth experiments at room temperature, the cycle frequency is 5 Hz.

Test mark [−]	Angle [°]	Loading axis	$F_{max,HCF}$ [kN]	$F_{max,LCF}$ [kN]	Cycle-ratio HCF:LCF	$\Delta K_{I,a\,=\,1.5mm,\,HCF}$ [MPa√m]	$\Delta K_{I,a\,=\,1.5mm,\,LCF}$ [MPa√m]
sBJRTdf3	45	A & B	35/17.5	-	-	-	-
mAARTdf1	0	B	13.0	-	-	20	-
mAARTdf3	45	A & B	18.0	-	-	20	-
mAARTdf5	45	A & B	18.0	35.5	20:1	20	40

through the load-introduction arms of axes A and B, where the specimen centre section has a diameter of 15 mm and a thickness of 1.8 mm. In order to perform fatigue crack growth experiments and induce crack growth at a certain location, a crack-starter notch is manufactured through wire electrical discharge machining with two different orientations.

The planar biaxial test rig uses an Instron 8800 control unit and four servo-hydraulic cylinders (F_{max} = 250 kN) to build the two perpendicular load axes. The cruciform specimen is clamped in the centre of the machine. To avoid shear stresses acting on the pistons, the control technology ensures that the midpoint of the specimen is always stationary. With this configuration, the axis of the cruciform specimen can be independently loaded, and arbitrary loading ratios of axes A to B can be applied. The experimental setup is available at the Technical University of Darmstadt and is widely used to study creep-fatigue life or low cycle fatigue (LCF) lifetime when multiaxial stress states are applied.[23,24] For further details on the machinery, refer to the studies of McAllister and Kontermann.[25,26]

Table 1 lists the parameters of the loading scenarios for the measurements outlined in this paper. Trial sBJRTdf3 with quenched and tempered steel 26NiCrMoV14-5 (sBJ) uses variable loads to prove the generality of the evaluation concept at an s-shaped crack contour. The maximum force of 35 kN on axis A and 17.5 kN on axis B was applied in Figure 6. The other trials with the test mark 'mAA' use the titanium alloy Ti6246 for aero engine applications like blisks. The parameters of testing are outlined in Table 1. Equal testing conditions by means of a common amplitude ratio of $R = -1$ and sinusoidal loading with a frequency of 5 Hz were maintained. High cycle fatigue (HCF) loadings allow trials with more than 10,000 cycles. An ACPD probe served as a reference for crack length measurement. A linear correlation between the electrical resistance measured by ACPD and crack length is assumed.

Experiments mAARTdf1 and mAARTdf3 are carried out with a constant force-controlled loading amplitude (HCF), leading to a cyclic crack tip loading of 20 MPa$\sqrt{\text{m}}$ at an initial crack length of 1.5 mm, but to different values for the T-stress of −174.3 and 0.17 MPa, respectively. As ΔK increases with increasing crack length, such experiments can be used to derive constants in Paris diagrams. Usually, components such as turbine blades or blisks in aero-engines or gas turbines do not regularly experience only one amplitude of loading; the third experiment adheres to this. A component near load-collective is mimicked by two amplitudes of loadings within a fixed sequence in trial mAARTdf5. Within one cycle package, an HCF amplitude of 18 kN is applied for 20 consecutive cycles, followed by an overload LCF amplitude of 35.5 kN. The experiments are selected to demonstrate the functionality of the DIC system—An evaluation according to fracture mechanical theory is beyond the scope of this publication; it can be found in the study of Conrad et al.[20]

3 | GPU-BASED DIC-SENSOR

The left side of Figure 2 shows the sensor head of the real-time DIC system in front of the biaxial testing machine with a cruciform specimen from Figure 1. It consists of a sensor head combining a fast CoaXPress 2.0 camera (Optronis Cyclone 5–700 M) in combination with a coaxial 4 W LED light mounted on a telecentric lens with 1:1 magnification (VST VS-THV1-150CO/S, working distance 150 mm), resulting in an image resolution of 5 µm/pixel on the object side. A CoaxPress 2.0 frame grabber (Euresys Coaxlink Quad CXP-12) transfers image data from the camera to an Intel Core i9-7900 computer equipped with an Nvidia GeForce RTX 2080 TI GPU with 11 GB of RAM and 4352 CUDA cores. Compared to the system described in the study of Blug et al.,[13] this hardware combination increases the data transfer rate between camera and PC from 0.7 GB/s by a factor of five to roughly 3 GB/s, depending on the number of rows used. For biaxial strain-control, a field-of-view (FOV) 8.0 × 7.7 mm^2 (1600 × 1540 pixels) is acquired with a frame rate of 850 Hz, sufficient for a 1% resolution of triangular strain cycles of 4 Hz; for uniaxial strain-control, the FOV is reduced to 12.8 × 4.4 mm^2 (2560 × 880 pixels) to increase the frame rate to 1500 Hz. Apart from cross-contraction, out-of-plane motions are not relevant as the specimen is flat in the crack growth area and precision-guided in the testing machine. Therefore, 2D DIC is sufficient. In contrast to the study of Blug et al.,[13] the zero-normalised cross-correlation algorithm by Kaso was implemented on the GPU.[27]

The system is operated either in 'strain-control' mode, where integral strain over a base length of 10 mm is calculated along the A and B axes from four subsets, or in 'full-field' mode with up to 40,000 subsets for local strain calculations. Both cases are shown on the right side of Figure 2, where a camera image is superimposed by the four subsets for strain-control and the full-field DIC area surrounding the crack-starter notch. For large cracks with a total length of up to 7 mm (2 a), the outer subsets must have a sufficient distance to the crack to measure global strain along the A and B axes independent from crack length. As FEM simulations indicate, the minimum base length l_0 for strain calculation is 10 mm, similar to that of the mechanical extensometer. To optimise the frame rate for a given image data transfer rate of 3 GB/s, the camera was tilted by 45°. Thus, the A and B axes run diagonally, so that a FOV of 8.0 × 7.7 mm^2 yields a sufficient base length. The resolution of 5 µm/pixel on the object side is sufficient for marker-free measurements on many metal surfaces, including cast aluminium, eroded surfaces and polished steel.

4 | CLOSED-LOOP OPERATION FOR CRACK GROWTH

The green outer subsets in Figure 2b for strain-control consist of two concentric squares: the inner ones mark the area of the reference templates (typically 63 × 63 pixels), and the outer ones determine the so-called search areas with typically 127 × 127 pixels within that displacement is measured path-independently, that is, without tracking. This path-

independence makes strain-control robust against single mismeasurements potentially interrupting tracking because it does not depend on previous images or evaluation results.[16] Furthermore, the sample surface is not speckle-painted, as it is necessary for most commercial systems.[28] Instead, it works marker-free by correlating the microstructure of the specimen surface with a repeatability for load-free in-plain translations in the range of 0.1 µm for a broad variety of metal surfaces like cast iron, eroded surfaces or polished steel—corresponding to 10 microstrains at a base length of 10 mm. To remain compatible with standard PID controllers such as the Instron 8800, it has to generate 10 V analogue elongation signals for feedback. Figure 3 shows the functional diagram of this double purpose sensor.

Figure 4 shows the response of the closed-loop system from Figure 3 to triangular strain curves with an amplitude of 10 µm on the faster B-axis and of 0 µm on the A-axis, compensating transverse contraction. On the left, elongation signals $\Delta \boldsymbol{l}_A(\boldsymbol{t})$ and $\Delta \boldsymbol{l}_B(\boldsymbol{t})$ are drawn together with force signals $F_A(t)$ and $F_B(t)$ from the PID controller for a cycle frequency of 1 Hz. On the right, at 5 Hz cycle frequency, the signal becomes more sinusoidal due to the large mass of the biaxial test site. However, the loop is rather complex as the PID controller has to translate the elongation signals $\Delta \boldsymbol{l}_A(\boldsymbol{t})$ and $\Delta \boldsymbol{l}_B(\boldsymbol{t})$ to forces for each axis by the PID controller. These forces are again transformed into positions for each axis, respecting that they depend on each other by the motion centre and by the transverse contraction of the sample. The biaxial testing machine thus forms a cascaded closed-loop where the B-axis is positioned first with symmetry to the sample centre and the A-axis corrects the interdependencies between both axes. Some more details are described by

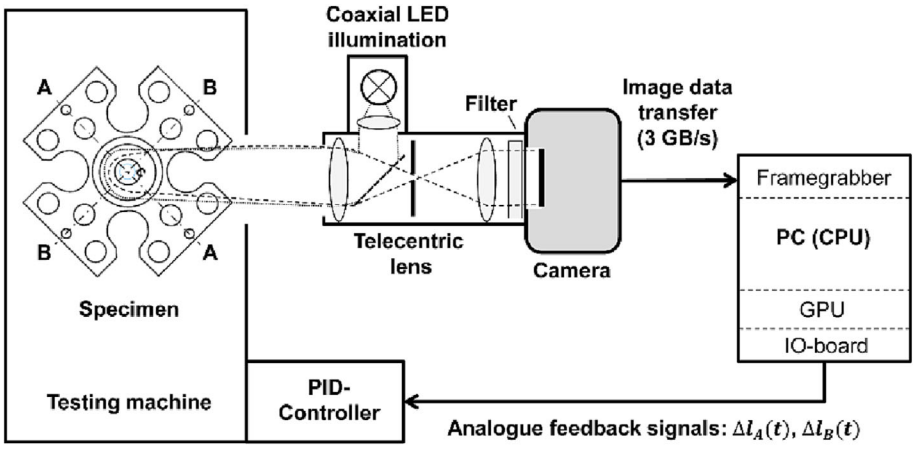

FIGURE 3 Functional diagram of the closed-loop system for strain-controlled crack growth. The digital image correlation (DIC) system delivers similar analogue elongation signals as mechanical extensometers, so that it is able to replace them in uniaxial and biaxial material testing.

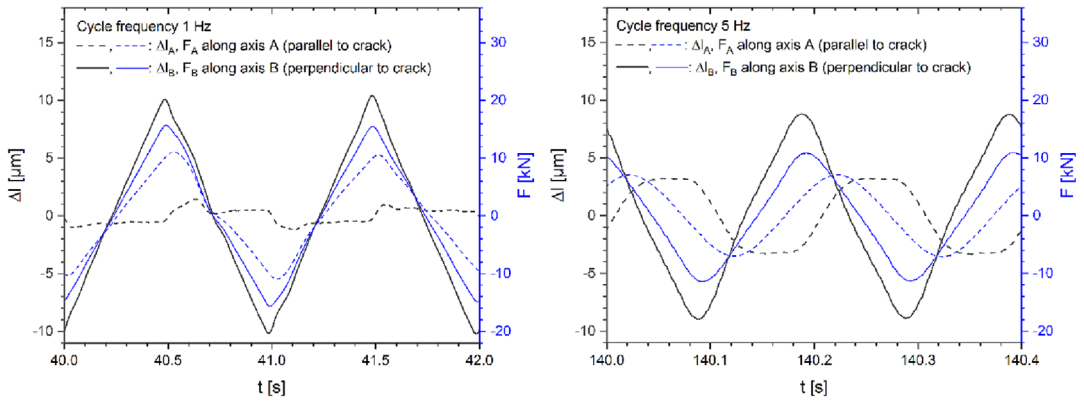

FIGURE 4 Optically strain-controlled experiments with a 7 mm crack parallel to the A-axis as perturbation. The graphs show the elongation signals obtained for set points of 0 and 10 µm for elongation amplitudes on axes A and B, respectively, for cycle frequencies of 1 Hz (left) and 5 Hz (right).

Kontermann.[26] Large cracks form a step-perturbation for the closed-loop system as the stiffness of the sample changes abruptly when the crack opens or closes. Therefore, the specimen with a 7 mm crack parallel to the A-axis as shown in Figure 4 demonstrates the stability of the closed-loop system in a worst-case situation. Please note that the force and strain signals from Figure 4 can also be used to measure crack opening/closing force by this crack-induced change in stiffness by the compliance method.[1]

5 | IMAGE PROCESSING WORKFLOW

Although both integral strain and full field are in principle accessible in real-time, crack growth evaluation starts with measuring the crack path in the maximum force or strain image from the last cycle of an experiment, where it is best known. Within that displacement field, a crack path $p(s)$ for the complete trial is measured, along which crack tip positions are searched for every cycle. The images and signals necessary to do that are collected in real-time in strain-control mode using the signals from Figure 4. The resulting workflow is sketched in Figure 5, together with the amount of involved data from the example of trial mAARTdf5.

Within trial mAARTdf5, 8.36 million images or 21 TB of image data are processed in 'strain-control' mode within 4:45 h. 0.16 TB (0.7%) of images are stored for post processing, about 1200 to measure crack length a. As it is a special trial with mixed HCF and LCF loads, the images of 575 cycles—two HCF cycles before and after 115 LCF cycles—are stored completely for a detailed evaluation of crack opening/closing behaviour.[29] After the trial, automated post-processing is started for the full-field evaluation described subsequently. The postprocessing time is divided into 14 min on the GPU for full-field DIC processing of 1200 images and another 15 min to process the crack growth results shown in Figure 7 in a Python script.

6 | FULL-FIELD EVALUATION OF BIAXIAL CRACK CONTOUR

For full-field calculation with many subsets, the correlation rate of the GPU of about 74 kHz becomes the limiting bottleneck. In this case, 40,000 subsets are evaluated within 540 ms. The coordinates (x,y) and (A,B) of the camera and the machine or FEM coordinate systems are transformed by equation

$$\begin{pmatrix} A \\ B \end{pmatrix} = \frac{1}{\sqrt{2}} \begin{bmatrix} 1 & -1 \\ -1 & -1 \end{bmatrix} \begin{pmatrix} x \\ y \end{pmatrix} + \begin{pmatrix} A_0 \\ B_0 \end{pmatrix}. \tag{1}$$

The vector (A_0,B_0) describes the offset between the origins of both systems. Similarly, the displacements $\vec{u}$ are transformed from camera coordinates to those of the testing machine:

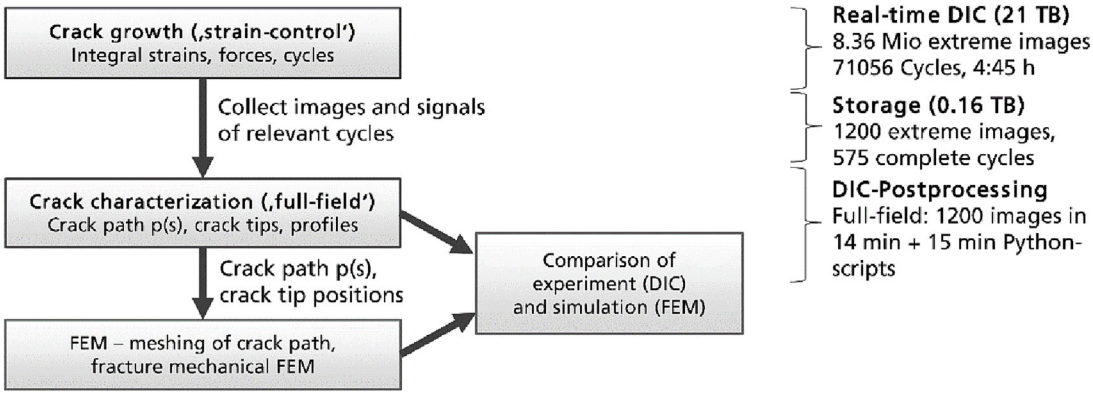

FIGURE 5 Workflow for digital image correlation (DIC) crack growth evaluation together with the corresponding amount of image data from trial mAARTdf5.

$$\begin{pmatrix} u_{A,DIC} \\ u_{B,DIC} \end{pmatrix} = \frac{1}{\sqrt{2}} \begin{bmatrix} 1 & -1 \\ -1 & -1 \end{bmatrix} \begin{pmatrix} u_x \\ u_y \end{pmatrix}. \tag{2}$$

In camera coordinates, the symmetrical local strain tensor $\bar{\bar{\varepsilon}}(x,y)$ is calculated from the local displacement $\vec{u}(x,y)$ using the derivative operators $\frac{\partial}{\partial x}$ and $\frac{\partial}{\partial y}$ along the axes of the system[30]:

$$\bar{\bar{\varepsilon}}(x,y) \equiv \begin{bmatrix} \varepsilon_x & \varepsilon_{xy} \\ \varepsilon_{xy} & \varepsilon_y \end{bmatrix} = \begin{bmatrix} \frac{\partial}{\partial x} u_x(x,y) & \frac{1}{2}\frac{\partial}{\partial y} u_x(x,y) + \frac{1}{2}\frac{\partial}{\partial x} u_y(x,y) \\ \frac{1}{2}\frac{\partial}{\partial y} u_x(x,y) + \frac{1}{2}\frac{\partial}{\partial x} u_y(x,y) & \frac{\partial}{\partial y} u_y(x,y) \end{bmatrix}. \tag{3}$$

To maximise spatial information according to Nyquist's theorem in full-field mode, the spacing between neighbouring subsets is chosen as half subset size, that is, 8 pixel or 40 µm for 15 × 15 pixels subsets (75 µm subset size), resulting in an overlap of about 50% in every direction. As cracks are discontinuities in local displacement, normalised Sobel-like operators S_x and S_y operating on 5 × 5 subsets are used as derivative operators:

$$S_x = \begin{bmatrix} 0 & 0 & 0 & 0 & 0 \\ -0.25 & 0 & 0 & 0 & 0.25 \\ -0.5 & 0 & 0 & 0 & 0.5 \\ -0.25 & 0 & 0 & 0 & 0.25 \\ 0 & 0 & 0 & 0 & 0 \end{bmatrix}, S_y = \begin{bmatrix} 0 & -0.25 & -0.5 & -0.25 & 0 \\ 0 & 0 & 0 & 0 & 0 \\ 0 & 0 & 0 & 0 & 0 \\ 0 & 0 & 0 & 0 & 0 \\ 0 & 0.25 & 0.5 & 0.25 & 0 \end{bmatrix}. \tag{4}$$

The strain tensor in Equation (3) is calculated by the convolution of the displacement field $\vec{u}(x,y)$ with the derivative operators

$$\frac{\partial}{\partial x} \equiv \frac{1}{l_S} S_x, \frac{\partial}{\partial y} \equiv \frac{1}{l_S} S_y, \tag{5}$$

where l_S is the diameter of the convolution kernels S_x and S_y, that is, four times the subset spacing of 8 pixel or about 160 µm. As l_S is larger than the subset size of 75 µm, the non-zero elements of S_x and S_y become non-overlapping. This is important for correct displacement measurement as those subsets traversed by the crack are not correlated correctly. If these operators are applied to an area containing an opened crack, a minimum of two non-zero elements of S_x and S_y lie on either side. Therefore, simple median filtering is sufficient to obtain the displacement fields shown in Figure 6. Please note the similarity of these derivative operators to the non-linear ones proposed by Feld-Payet.[10]

However, for the strain transformation from camera coordinates (x,y) to biaxial coordinates (A,B), the inner derivatives must be considered. For a tilt angle of 45°, the transformation of the components of the strain tensor $\bar{\bar{\varepsilon}}(A,B)$ becomes

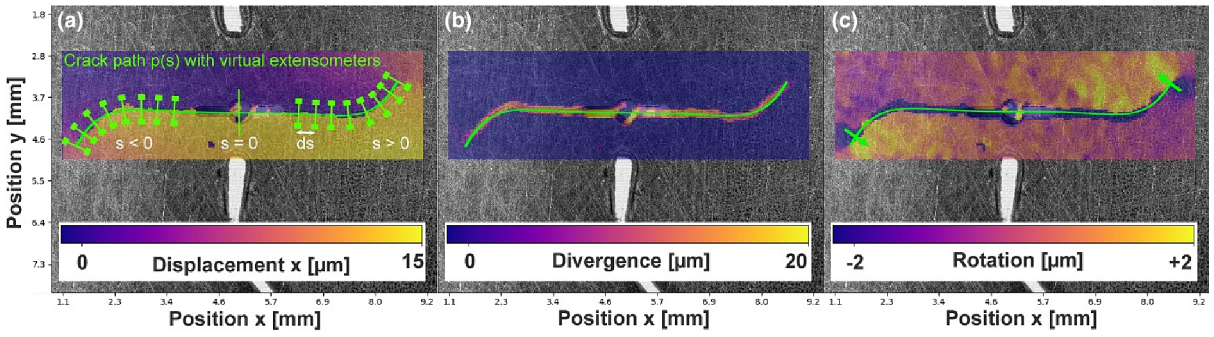

FIGURE 6 Full-field analysis of experiment sBJRTdf3. (a) Displacement in x-direction (y-direction is similar) with crack path p(s) (green lines) and virtual extensometers. (b) Divergence of the displacement field. (c) Rotation of the displacement field. The green arrows mark the extrema of the rotation gradients perpendicular to the crack contour for crack tip detection.

$$\varepsilon_A = \frac{1}{2}\varepsilon_x + \frac{1}{2}\varepsilon_y + \varepsilon_{xy}; \varepsilon_B = \frac{1}{2}\varepsilon_x + \frac{1}{2}\varepsilon_y - \varepsilon_{xy}; \varepsilon_{AB} = \frac{1}{2}(\varepsilon_y - \varepsilon_x). \tag{6}$$

The arguments (x,y) are transformed using Equation (1). With this equation, it is easy to show that the divergence $div\,\vec{u}$ known from the J-integral is a coordinate system and direction-independent measure for displacement at the crack contour:

$$div\,\vec{u} \equiv \frac{\partial u_x}{\partial x} + \frac{\partial u_y}{\partial y} = \varepsilon_x + \varepsilon_y = \varepsilon_A + \varepsilon_B \tag{7}$$

As discussed below, the rotation $rot\,\vec{u}$ of the displacement field $\vec{u}$ can be used for crack tip localisation:

$$rot\,\vec{u} \equiv \frac{\partial u_y}{\partial x} - \frac{\partial u_x}{\partial y} \tag{8}$$

The rotation exhibits maxima and minima near the crack tip because the direction of the displacement vectors changes. Thus, the 'gradient', that is, the slope within the rotation field perpendicular to the crack growth direction, should be a load-independent candidate to detect crack tip position, which worked well on uniaxial trials.[19]

Figure 6 illustrates how these operations are used to measure crack path and crack flank displacements in full-field mode in the example of a rather complex biaxial crack contour. The measurement is taken at maximum force from the last cycle of a biaxial crack growth experiment sBJRTdf3 with a variable load. Figure 6 shows the displacement $u_x(x,y)$ in the coordinates of the strained image so that the displacement field fits into the image acquired under load. The crack appears as a discontinuity in the displacement field, decreasing continuously towards zero at the crack tips. To obtain the crack path $p(s)$ (green lines), a fixed threshold of 1.5 µm is applied to divergence $div\,\vec{u}$ in Figure 6b and fitted by a polynomial—in this case of 7th degree. Along that path, an arbitrary number of virtual extensometers is distributed automatically at a distance ds (typically between 10 and 100 µm) to measure the following profiles: crack flank displacement $u_I(s)$ in mode I direction perpendicular to the path; crack flank displacement $u_{II}(s)$ in mode II direction (parallel); divergence profile $div\,\vec{u}(s)$; and the gradient of the rotation profile $rot\,\vec{u}(s)$ perpendicular to path $p(s)$. The advantage of the latter profile is that the positions of maximum and minimum gradients marked by the green arrows in Figure 6c are expected to be load-independent. The distance of the extensometer subsets (green squares) to the crack path is about 200 µm, slightly larger than l_S.

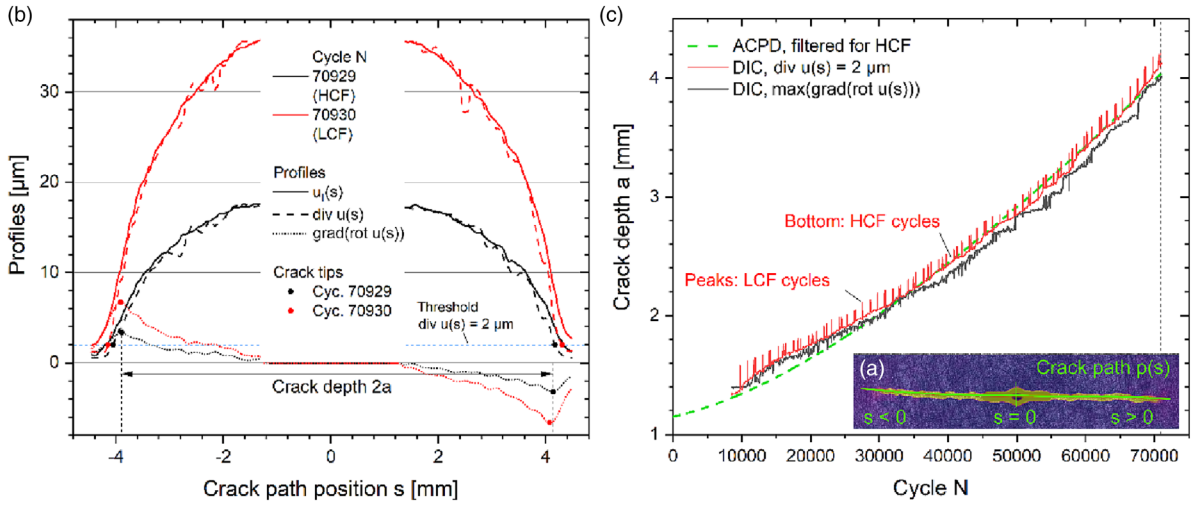

FIGURE 7 (a) Crack path $p(s)$ (green line) fitted to a horizontally growing crack. (b) Profiles $u_I(s)$, $div\,\vec{u}(s)$ and $grad\left(rot\,\vec{u}(s)\right)$ measured at position s along crack path $p(s)$ for a high cycle fatigue (HCF) (black) and a low cycle fatigue (LCF) cycle (red). The dots mark the crack tip positions. (c) Crack lengths a measured in trial mAARTdf5 with mixed HCF and LCF cycles by alternating current potential drop (ACPD), by thresholding $div\,\vec{u}(s)$, and as $\max\left(grad\left(rot\,\vec{u}(s)\right)\right)$.

Both divergence and rotation are derivative operators that are unitless according to Equations (5)–(8), whereas their units in Figure 6 are 'micrometre'. The reason is that the discontinuity due to crack opening—which is independent from l_S—dominates the displacement at the crack, whereas the effects of strain are negligible. Therefore, the results of S_x and S_y are plotted without division by l_S to avoid a dependency on subset size. As discussed in Figure 7b, this enables the use of divergence as a direction-independent measure for crack opening.

Crack length a is measured as half the length of the polynomial between the crack tips. Consequently, crack path position s is chosen to be zero at the notch centre and positive at larger x values. Figure 7 illustrates two options to measure crack tip position for a trial with variable HCF and LCF loads (mAARTdf5). Figure 7a shows the crack path $p(s)$ fitted to divergence $div\left(\vec{u}\right)$. Along this path, crack flank displacement $u_I(s)$, divergence profile $div\,\vec{u}(s)$ and the gradient of the rotation profile $rot\,\vec{u}(s)$ are plotted for $ds = 100\,\mu m$ in Figure 7b. Please note that $u_I(s)$ and $div\,\vec{u}(s)$ are quite similar measures for crack flank displacement. The major difference between them is that $u_I(s)$ is measured at the subsets at the ends of the virtual extensometers, that is, 200 µm on either side of $p(s)$, whereas $div\,\vec{u}(s)$ is calculated from subsets much closer to the crack. Therefore, $div\,\vec{u}(s)$ is more affected by edges in the real crack that are smoothed by the polynomial, for example, at grain boundaries, whereas $u_I(s)$ is affected by different deformations at the crack tip like shear, typically occurring at distances larger than half the Sobel diameter l_S.

Within these profiles, crack tip positions were determined in two different ways: either by interpolating $div\,\vec{u}(s)$ to a fixed threshold Δu of 2 µm or by measuring the minimum and maximum positions of the gradient profiles $rot\,\vec{u}(s)$. Figure 7c shows the evolution of these measures for crack length a over 60,000 cycles under HCF and LCF loadings in comparison to ACPD values, which are already filtered for HCF cycles.

As expected, crack length from divergence is load-dependent. The peaks in the crack lengths from $div\,\vec{u}(s)$ (red curve in Figure 7c) result from LCF cycles: doubling the load means an increase of about 0.2 mm. Nevertheless, the crack extension da is constant for either load, so that absolute crack length a can be calibrated from microscopy before and after the trial as the ACPD signal. DIC crack length from $rot\,\vec{u}(s)$ does not show any correlation with LCF cycles because it is load-independent. As discussed for Figure 9, it turned out to be more sensitive local 'waves' in the displacement $\vec{u}$. Therefore, crack lengths are measured from divergence profiles $div\,\vec{u}(s)$ subsequently.

7 | COMPARISON BETWEEN DISPLACEMENTS MEASURED BY DIC AND CALCULATED BY FEM

As stated in the introduction, fracture mechanical FEM simulations are required to obtain the stress intensity factor K at the crack tips for a crack path $p(s)$ measured by full-field DIC. Because of the low thickness in the centre of the specimen, plane-strain conditions are assumed to be prevalent over the whole cross section. With this adaptation, a suitable two-dimensional model was established, which requires less meshing effort and calculation resources than a three-dimensional one. Therefore, it was possible to automatically adapt the FEM mesh within a Python script to the crack paths measured by DIC. The modelling strategy will be outlined in the following, starting with Figure 8. The left side of Figure 8 shows the cross section along axis A through the centre of the specimen geometry. Within the two-dimensional reduction of the concave tapering towards the centre, the specimen is discretised as areas with constant thicknesses in a first step. The right side of the cross section shows the explained approximation with overlaid

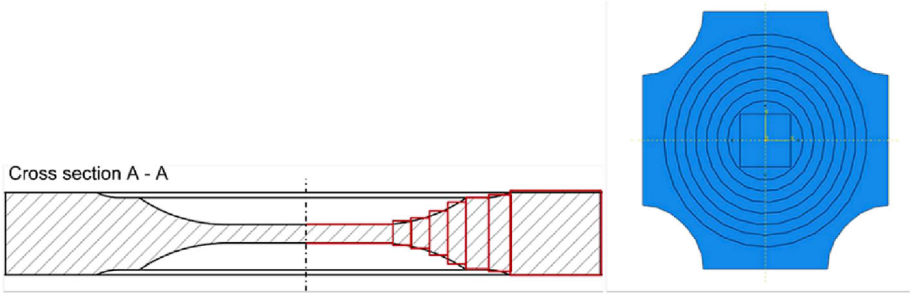

FIGURE 8 Cross-section of cruciform geometry through the centre (left), indicating the approach of discretization. 2D finite-element model (FEM) (right).

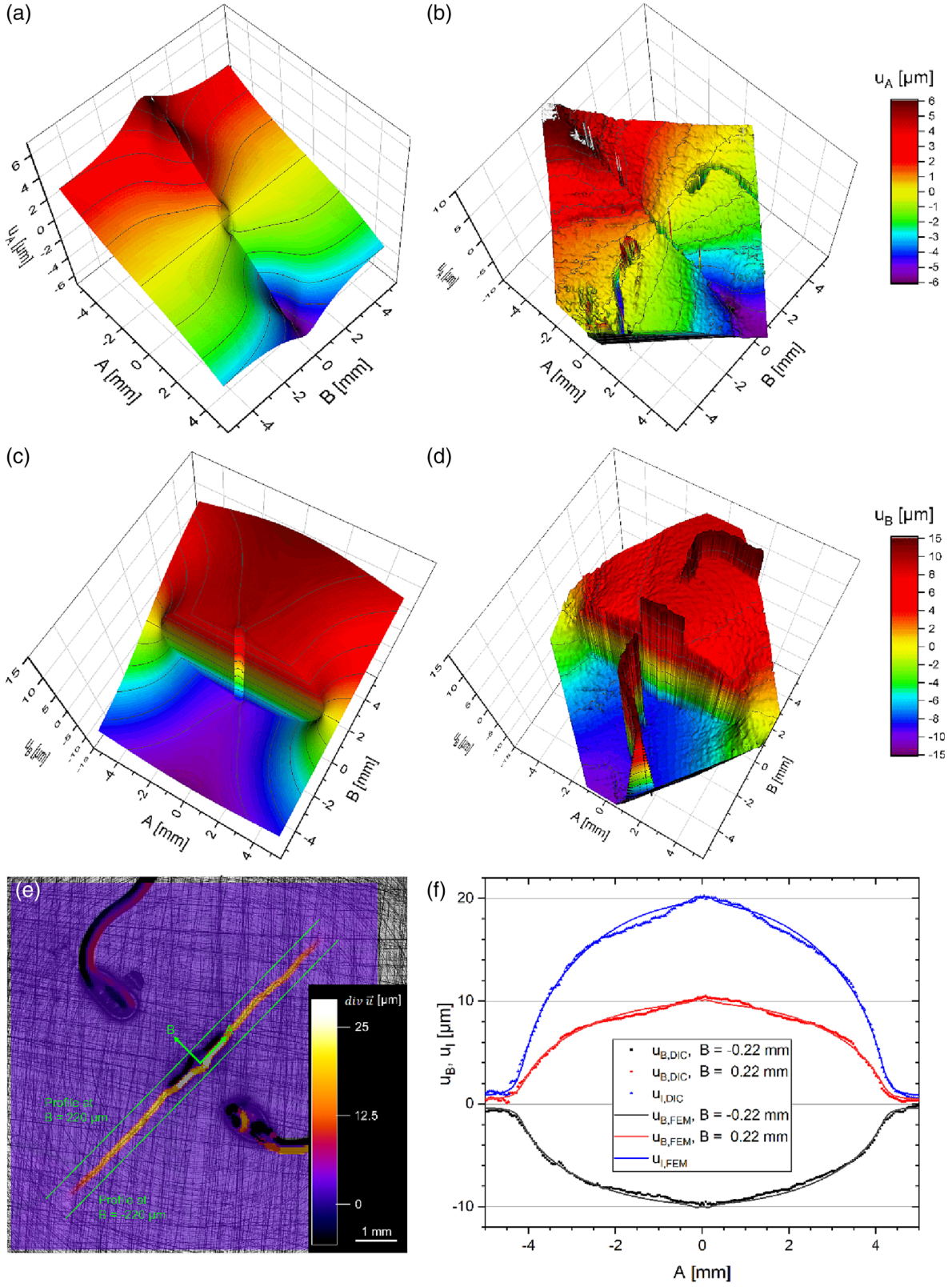

FIGURE 9 Comparison of full-field digital image correlation (DIC) measurement and fracture mechanical finite-element model (FEM) calculated from DIC crack path $p(s)$ (trial mAARTdf1). 3D views of displacements $u_{A,FEM}$ (a), $u_{A,DIC}$ (b), $u_{B,FEM}$ (c) and $u_{B,DIC}$ (d). (e) Overlay of camera image and DIC divergence of the crack growing along axis A. (f) Profiles from $u_{B,DIC}$ (red and black dots) and $u_{B,FEM}$ (red and black lines) along the green lines in e, that is, ±220 µm from the crack. The blue crack opening profiles $u_{I,DIC}$ and $u_{I,FEM}$ are the differences between the red and black DIC and FEM profiles.

rectangles and their respective thickness. In a second step, a 2D-planar-shell-model in the FEM Software Abaqus™ is generated (Figure 8, right). The discretised areas of tapering are modelled as two-dimensional sections with the respective thickness lodged for plane stress/strain calculations. The sections appear as rings on the top view of the model and lead to an approximate relationship between the external forces and the prevalent stresses and strains in the centre. The simulation is carried out with the respective testing force amplitudes under consideration of linear-elastic material behaviour. The only material parameters required are Young's modulus and Poisson ratio obtained by tensile testing.

The resulting distributions of strain or displacements can, in principle, be compared with those measured by DIC.[19] However, in the plastic zone, strain values differ in magnitude and size because of different effects: first, a linear-elastic material behaviour was considered, leading to an overestimation in the FEM simulation due to missing plasticity, whereas DIC measures total strain.[31] Second, the resolution of both evaluations differs. The FEM mesh uses an element size of 2.5 µm at crack tip, whereas the length l_S for the DIC derivatives in Equation (6) is 160 µm due to subset spacing and Sobel kernels given in Equation (4). Therefore, we compared total displacements on the specimen surface as they are directly measured by DIC and incorporate the response of the mechanical behaviour of the material in bulk. The displacements in these areas are also used for the estimation of ΔK from DIC, either by COD[8] or by J-integral.[31]

Figure 9 shows a comparison of FEM and DIC displacements along axes A and B from trial mAARTdf1 after 80,358 cycles according to the post-processing workflow given in Figure 5. First, the crack contour is extracted from the images taken at maximum load and transferred to the FEM. For this contour and load (13 kN on axis B), the displacements $u_{A,FEM}$ and $u_{B,FEM}$ drawn as 3D views in Figure 9a,c are calculated. Within the 3D surfaces, the discontinuities of the displacements at the cracks appear as vertical walls along the crack contour. Please note, that only the central hole of the crack starting notch was simulated within FEM. Similarly, the corresponding DIC displacements $u_{A,DIC}$ and $u_{B,DIC}$ for the same crack are drawn in Figure 9b,d. As the crack grows along axis A, displacement fields $u_{A,FEM}$ and $u_{A,DIC}$ contain the mode II displacements, and fields $u_{B,FEM}$ and $u_{B,DIC}$ the corresponding mode I displacements. With some exceptions at the crack starting notch and in the proximity of the ACPD contacts—which are both excluded from the FEM—they show very similar contours, and the deviations are well below 1 µm. Within the DIC data, there are also some spikes along the crack resulting from those subsets traversed by the crack. These spikes can be easily removed by 5×5 median filtering prior to the divergence or rotation calculation. In addition, the DIC data exhibits a local 'waviness' in the flat parts outside the crack arising from local inhomogeneities within the material and from DIC noise. As the gradient of the rotation $rot\,\vec{u}$ is the difference between two derivatives, this waviness alters the maxima in the profiles $grad(rot(u(s)))$ in Figure 7b and therefore the corresponding crack length drawn in Figure 7c. Sometimes, multiple maxima appeared near the crack tip position, resulting in ambiguous crack lengths.

To obtain a more quantitative comparison between the FEM and DIC measurement, profiles of the displacements $u_{B,FEM}$ and $u_{B,DIC}$, that is, in mode I direction, are drawn in Figure 9f. The position of these profiles is indicated by the green lines within the overlay of the divergence and the camera image in Figure 9e, that is, at a distance of 220 µm on either side of the crack. So, the tips of the virtual extensometers in Figure 6 lie close to these lines, and the profiles are just outside the crack starting notch. The black dots and the black line mark the $u_{B,DIC}$ and $u_{B,FEM}$ values at $B = -220$ µm, respectively, and the red ones those at $B = 220$ µm. Within these profiles, the maximum deviation is 0.6 µm in the area of the crack starting notch and the standard deviation is 0.25 µm. The difference between the red and the black profiles in Figure 9f results in the crack opening profiles $u_{I,DIC}$ (blue dots) and $u_{I,FEM}$ (blue line) in the mode I direction, comparable to the profiles $u_I(s)$ in Figure 7b. The maximum deviation between $u_{I,DIC}$ and $u_{I,FEM}$ is 0.75 µm near the ends of the crack starting notch (which is masked out in Figure 7b), and the standard deviation of the difference $\Delta u_I = u_{I,DIC} - u_{I,FEM}$ is 0.36 µm. In the rising and falling parts at $-4\,\text{mm} < A < -3\,\text{mm}$ and $3\,\text{mm} < A < 4\,\text{mm}$, respectively, which are typically used to calculate the cyclic stress intensity factor ΔK, the agreement is even better. This means that both DIC measurement and FEM values calculated from DIC crack path $p(s)$ are consistent and can be used to calculate the cyclic stress intensity factor ΔK for the Paris diagram in the subsequent section.

8 | COMPARISON BETWEEN CRACK LENGTHS MEASURED BY DIC AND ACPD

The purpose of fatigue crack growth experiments is to derive the relation between applied crack tip loading and crack growth rate. The mutual relationship is commonly described by the Paris equation, whose material parameters are determined from experiments with constant amplitude loading like trial mAARTdf3. This trial uses the same HCF parameters like mAARTdf5 so that the results can be compared to Figure 7c.

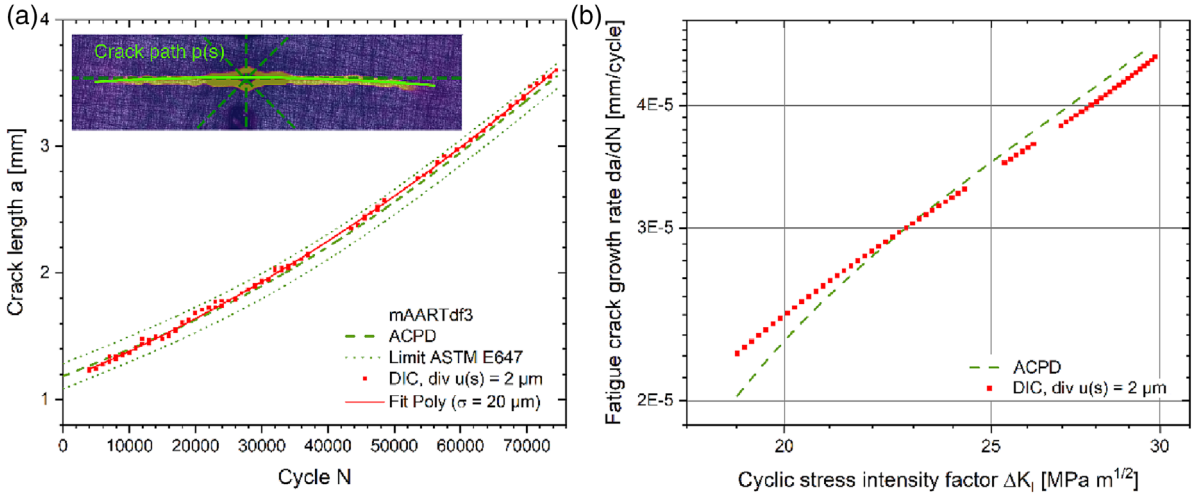

FIGURE 10 (a) Comparison of alternating current potential drop (ACPD) (dashed line) and digital image correlation (DIC) crack lengths a by thresholding $div\,\vec{u}(s)$ (red dots) from trial mAARTdf3. Both agree within the ASTM E647 limit of ±0.1 mm (dotted lines). (b) Paris diagram from both datasets using ΔK_I values in mode I direction calculated by finite-element model (FEM).

Figure 10a shows crack lengths a from ACPD as a reference and from DIC by thresholding $div\,\vec{u}(s)$ as described in Section 6. Both agree well within the limit of ±0.1 mm (standard deviation) recommended by ASTM E347. Please note that the 124 DIC measurements were taken without interrupting the experiment. To obtain a smooth derivative da/dN, a 2nd degree polynomial (red line) was fitted to the DIC crack length. The root mean square (RMS) value σ of the fit was 20 µm, which might serve as a measure for the reproducibility of DIC crack length measurement. Because of the interpolation of the profile $div\,\vec{u}(s)$, the reproducibility is well below subset size (75 µm) and the diameter $l_S = 160$ µm of the Sobel operator. DIC crack length after cycle 74,536 was 3.598 mm, that is, 43 µm above microscopy measurement of 3.555 mm for ACPD calibration.

Cyclic stress intensity factors ΔK_I in mode I direction were calculated by the FEM in steps of 0.1 mm for crack length along DIC crack path $p(s)$. The result is the Paris diagram for both datasets shown in Figure 10b. Here, the DIC data is in good agreement with the ACPD data, demonstrating again the consistency. A comparative study of mAARTdf1 and mAARTdf3 including crack opening by compliance method to calculate the effective stress intensity factor $\Delta K_{I\,eff}$ and the influence of T-stress was published in the study Conrad et al.[1,20]

9 | DISCUSSION AND OUTLOOK

Real-time DIC has the potential to replace several sensors in standard crack growth experiments, like mechanical extensometers for integral strain, ACPD for crack length and mouth opening gauges—in particular, if it works marker-free, that is, without preparation of the specimen with a speckle pattern.[28] On top, it provides additional information such as displacement images similar to those calculated by FEM, which are, for instance, of particular interest for crack driving force determination. Therefore, it enables a comprehensive evaluation of biaxial fatigue crack growth experiments, which is important for a precise determination of the remaining service life of technical components.

This paper describes the application of a GPU-based real-time 2D DIC system to make some important steps in that direction. First, a camera is required, which gives sufficient spatial resolution for the crack tip over the FOV necessary for integral strain. Second, integral strain must be measured in real-time during crack growth, resolving 2% of the strain amplitude, that is, with a frame rate of 100 times the cycle frequency of 5 Hz. This requirement is met by a fast CoaXPress 2.0 camera acquiring more than 3 GB/s of image data sufficient to resolve 8.0 × 7.7 mm^2 images with 5 µm/pixel and a frame rate of 850 Hz in the biaxial case and 12.8 × 4.4 mm^2 ones with the same resolution and 1500 Hz in uniaxial trials. So the integral strain measurement rate is about an order of magnitude faster than other real-time DIC systems[13–17] because it is optimised for the exchange of many small data packets between CPU and GPU with low latency under closed-loop conditions. As demonstrated in Figure 4, the temporal resolution of 850 Hz with a latency of about 3 ms enables strain-controlled crack growth in a worst-case situation on this test site. The suitability of the spatial

resolution for crack length measurement is demonstrated in Figure 10a. In general, a resolution of 5 μm/pixel appears adequate on most metallic surfaces to use their microstructure for marker-free correlation. This makes it easier to track the crack tip because delamination is avoided. The subset size of 75 μm should be enough to resolve the plastic zone near the crack tip.[20,31]

As those experiments run for several hours, terabytes of image data must be handled. Here, real-time processing fulfils two purposes: it provides integral strain with a latency of about 2 ms to control the crack growth process like a mechanical extensometer, and it helps to select the relevant images for crack characterisation, which is executed here in an automated postprocessing step. Because of GPU acceleration, 1200 full-field images were processed in less than 30 min. For the complete crack growth experiment, the execution time is significantly shortened because the DIC system avoids many interruptions otherwise necessary to control the current state of crack growth.

In full-field mode, the same path-independent DIC implementation is used as in strain-control mode. Instead of calculating the correlation on 15 × 15 pixel subset size and exploiting the common information of neighbouring subsets, the correlation is calculated for the full 63 × 63 pixel search areas, covering the complete motion of every individual subset, that is, up to 25 pixel in every direction, with a correlation rate of 74 kHz. The result of this approach is excellent displacement data quality along the crack on the one hand, but also unnecessary computational redundancy in the overlapping areas of neighbouring subsets, in particular further away from the crack. This strategy is simple and data-efficient in the sense that every image of the crack growth trial can be directly compared to the reference image. Therefore, no intermediate images have to be stored, and application-specific tracking algorithms, which usually depend on crack path, are avoided. Alternatively, hierarchical (or pyramidal) Lukas-Kanade-based approaches like the FOLKI implementation might be used to avoid redundancy between neighbouring subsets in a path-independent way.[32] Besnerais et al. report to evaluate 2048 × 2048 pixel images with 31 × 31 pixel subsets on a Nvidia Titan GPU in 0.2 s for 2D DIC. As they assign a displacement value to every pixel, this corresponds to an evaluation rate of approximately 20 MHz if all displacement vectors are counted. However, according to Nyquist's theorem, spatial information is maximised at steps of half subset size, that is, 16 pixel. Counting only these displacements, the evaluation rate corresponds to 82 kHz, which is quite comparable to 74 kHz if the smaller correlation size (31 × 31 instead of 63 × 63 pixels) and the slightly slower GPU are considered. The FOLKI approach can deal with larger displacements of up to 250 pixels, whereas our approach provides fast integral strains with low latency for strain-controlled crack growth, for real-time image selection, and for the determination of crack opening/closing forces in addition to full-field information. Both implementations use zero-order shape functions, which are sufficient for deformations occurring in fatigue trials. For comparison, Thiagu et al.[12] report a correlation rate of about 1.5 kHz for a GPU-based DIC implementation with 21 × 21 pixel subset size, allowing for an iterative evaluation of higher-order shape functions as they are required for more complex deformations—which, according to the authors, is still a speedup by a factor of 9 compared to CPU implementations.

Measuring the crack length a of biaxial cracks in full-field DIC requires a direction-independent measure for crack path detection. This was accomplished by using the divergence as an omnidirectional measure for the discontinuity in the displacement. To determine the crack tip position along that path, two methods are discussed: thresholding the divergence profile or, alternatively, detecting the maximum rotation of the displacement vector. As crack opening is load-dependent, the crack length measured by thresholding is load-dependent, too, as demonstrated by a mixed HCF–LCF experiment. However, the rotation was found to be less robust against local variations of the displacement field. As the crack extension da appears to be correct, the absolute crack length is easily calibrated by a microscopy measurement, as it is done with ACPD and recommended by ASTM E647. This made us confident to use these techniques for a systematical study of the crack propagation behaviour of uniaxially loaded corner-crack specimens and biaxially loaded cruciform specimens from steel and titanium.[20,22] Because of its robustness, thresholding the divergence profile is our preferred method to measure crack tip position. The reproducibility, that is, the RMS value for polynomial fits, was usually in the range of 20 to 30 μm for a subset size of 75 μm.

The good agreement between DIC, FEM and ACPD as well as the robustness in trials with variable loads demonstrate that high-performance DIC has gained the maturity for widely automated crack growth experiments. Therefore, it has the potential to replace several sensors like mechanical extensometers, ACPD or mouth opening gauges in crack growth experiments in the future because it reduces the complexity of the setup while providing more information.

Although it is not yet integrated into the workflow, the computational power of a standard GPU is sufficient to give the operator of the test site a live view of Paris diagrams as feedback for the quality of the running experiment. In the case of unexpected events like the occurrence of secondary cracks, the stored images allow detailed investigations of the reason why they occurred.[22] When out-of-plane effects are negligible, as they are on most specimens with flat surfaces,

the GPU-based real-time 2D-DIC system is an excellent tool for a comprehensive evaluation of fatigue crack growth experiments.

ACKNOWLEDGEMENTS

The results presented are based on the IGF project 'Crack Behaviour Multiaxial (ARIMA)' supported by the Federal Ministry for Economic Affairs and Climate Action (BMWK) through the AiF (German Federation of Industrial Research Associations e.V.) based on a decision taken by the German Bundestag (IGF no. 20239 N, project duration 10/2018–03/2022). The authors would like to thank the Forschungskuratorium Maschinenbau e.V. and especially the FVV e.V. (FVV no. 6013251) for their support and working group. Special thanks to the Charmain, Dr. Andreas Fischersworring-Bunk (MTU Aero Engines AG), Ralf Lichtenberger (LIMESS Messtechnik u. Software GmbH) and all other industry members of the project steering committee. The final report is available online.[22] Open Access funding enabled and organized by Projekt DEAL.

DATA AVAILABILITY STATEMENT

The data that support the findings of this study are available on request from the corresponding author. The data are not publicly available due to privacy or ethical restrictions.

ORCID

Andreas Blug https://orcid.org/0000-0001-7702-1617

REFERENCES

[1] ASTM, *Standard Test Method for Measurement of Fatigue Crack Growth Rates, E647–15*, ASTM, West Conshohocken, PA Jul. **2016**.
[2] *Standard Test Method for Strain-Controlled Fatigue Testing*, ASTM E606, E08 Committee, West Conshohocken, PA **2012**.
[3] H. Schreier, J.-J. Orteu, M. A. Sutton, *Image Correlation for Shape, Motion and Deformation Measurements*, Springer US, Boston, MA **2009**.
[4] C. Roux-Langlois, A. Gravouil, M. C. Baietto, J. Réthoré, F. Mathieu, F. Hild, S. Roux, *Int. J. Solids Struct.* **2015**, *53*, 38. https://doi.org/10.1016/j.ijsolstr.2014.10.026
[5] S. Alshammrei, B. Lin, J. Tong, *Int. J. Fatigue* **2020**, *133*, 105449. https://doi.org/10.1016/j.ijfatigue.2019.105449
[6] J. Tong, *Fatigue Fract. Eng. Mater. Struct.* **2018**, *41*(9), 1855. https://doi.org/10.1111/ffe.12859
[7] J. Hebert, M. Khonsari, *Fatigue Fract. Eng. Mater. Struct.* **2022**, *1*(1), 33. https://doi.org/10.1111/ffe.13931
[8] M. Vormwald, Y. Hos, J. L. F. Freire, G. L. G. Gonzáles, J. G. Díaz, *Int. J. Fatigue* **2018**, *115*, 53. https://doi.org/10.1016/j.ijfatigue.2018.04.030
[9] J. Réthoré, *Int. J. Numer. Meth. Engng* **2015**, *103*(7), 516. https://doi.org/10.1002/nme.4905
[10] S. Feld-Payet, G. Le Besnerais, V. Bonnand, D. Pacou, L. Thiercelin, *Strain* **2020**, *56*(2), 7. https://doi.org/10.1111/str.12333
[11] T. Strohmann, D. Starostin-Penner, E. Breitbarth, G. Requena, *Fatigue Fract. Eng. Mater. Struct.* **2021**, *44*, 1. https://doi.org/10.1111/ffe.13433
[12] M. Thiagu, S. J. Subramanian, R. Nasre, *Strain* **2020**, *56*(3), 1. https://doi.org/10.1111/str.12342
[13] A. Blug, D. J. Regina, S. Eckmann, M. Senn, A. Bertz, D. Carl, C. Eberl, *Applied Sciences* **2019**, *9*(10), 2025. https://doi.org/10.3390/app9102025
[14] B. Pan, L. Tian, *Opt. Express* **2016**, *24*(17), 19082. https://doi.org/10.1364/OE.24.019082
[15] P. B. S. Bailey, M. Higham, *Procedia Structural Integrity* **2016**, *2*, 128. https://doi.org/10.1016/j.prostr.2016.06.017
[16] A. Moncy, J. P. Waldbjørn, C. Berggreen, *Exp Mech* **2021**, *61*(7), 1193. https://doi.org/10.1007/s11340-021-00725-6
[17] Y. Liu, K. Iwata, S. Sanda, M. Nishiyama, *J. Construct. Steel Res.* **2022**, *190*(9), 107166. https://doi.org/10.1016/j.jcsr.2022.107166
[18] A. Blug D. J. Regina, S. Eckmann, M. Senn, C. Eberl, A. Bertz, D. Carl, GPU-based digital image correlation system for real-time strain-controlled fatigue and strain field measurement, Proc. SPIE 11056-30, Optical Measurement Systems for Industrial Inspection XI, p. 30, **2019**. https://doi.org/10.1117/12.2525713
[19] F. Conrad, A. Blug, J. Kerl, J. Fehrenbach, D. J. Regina, A. Bertz, C. Kontermann, D. Carl, M. Oechsner, *Procedia Structural Integrity* **2020**, *28*, 2195. https://doi.org/10.1016/j.prostr.2020.11.048
[20] F. Conrad, C. Kontermann, A. Blug, A. Bertz, D. Carl, M. Oechsner, Influence of multiaxial far field loading on the fatigue crack-growth behaviour by using corner-crack and cruciform specimen, Proceedings of the ASME Turbo Expo 2022: Turbomachinery Technical Conference and Exposition. Rotterdam, Netherlands, June 13–17, 2022, Volume *8A*, GT2022-79394, **2022**.
[21] F. Conrad, A. Blug, D. J. Regina, J. Kerl, A. Bertz, C. Kontermann, M. Oechsner, Direction- and path-independent DIC strain-field evaluation for uniaxial and biaxial fatigue crack growth investigations, Proc. LCF9—Ninth international Conference on Low Cycle Fatigue, Berlin, **2022**.

[22] F. Conrad, C. Kontermann, A. Blug, FVV no. 1325|Final report (AB): Crack Behaviour Multiaxial (ARIMA): Verification, development and usage of models to assess the crack behaviour under multiaxial component near conditions. In Forschungsvereinigung Verbrennungskraftmaschinen—FVV e.V. (Hg.) 2022—Proceedings R603 of The FVV, pp. 742–776. [Online]. Available: www.fvv-net.de
[23] A. Simon, A. Scholz, C. Berger, Validation of creep fatigue lifetime calculation methods for the application to steam turbine rotors, Variable Amplitude Loading, Darmstadt, Proceedings, DVM, I, pp. 505–516, **2009**.
[24] A. Erbe, F. Conrad, K. M. Kraemer, C. Kontermann, M. Bianchini, D. Kulawinski, M. Oechsner, *Proc. Struct. Integr.* **2022**, *38*, 192.
[25] J. M. McAllister, The control of cruciform testing systems using opposed pairs of servohydraulic actuators, in *Seventh Bath International Fluid Power Workshop*, UK, Bath **1994**, 311.
[26] C. Kontermann, *Entwicklung und Validierung eines FEM-basierten Rissfortschrittsmodells zur Beschreibung von Stützwirkung unter Kriechermüdungsbeanspruchung. Dissertation*, TUprints, Darmstadt **2017**.
[27] A. Kaso, *PLoS ONE* **2018**, *13*(9), e0203434. https://doi.org/10.1371/journal.pone.0203434
[28] M. A. Sutton, F. Matta, D. Rizos, R. Ghorbani, S. Rajan, D. H. Mollenhauer, H. W. Schreier, A. O. Lasprilla, *Exp Mech* **2017**, *57*(1), 1. https://doi.org/10.1007/s11340-016-0233-3
[29] L. Patriarca, S. Foletti, S. Beretta, G. Hénaff, *MATEC Web Conf.* **2018**, *165*, 1001. https://doi.org/10.1051/matecconf/201816501001
[30] J. Rösler, H. Harders, M. Bäker, *Mechanisches Verhalten der Werkstoffe*, Springer Fachmedien Wiesbaden, Wiesbaden **2016**.
[31] E. Breitbarth, M. Besel, *Int. J. Fatigue* **2017**, *100*(1), 263. https://doi.org/10.1016/j.ijfatigue.2017.03.029
[32] G. Le Besnerais, Y. Le Sant, D. Lévêque, *Strain* **2016**, *52*(4), 286. https://doi.org/10.1111/str.12194

How to cite this article: A. Blug, F. Conrad, A. Bertz, C. Kontermann, D. Carl, M. Oechsner, *Strain* **2023**, *59*(6), e12455. https://doi.org/10.1111/str.12455